Hot Carriers-Induced Nonlinear Photoluminescence in Thin Indium Tin Oxide Layer Patterned by Ga Ion Beam Milling

Florian Dell'Ova, Konstantin Malchow, Rémi Chassagnon, Olivier Heintz, Nicolas Pocholle, Gérard Colas Des Francs, Erik Dujardin, Alexandre Bouhelier

Hot Carriers-Induced Nonlinear Photoluminescence in Thin Indium Tin Oxide Layer Patterned by Ga Ion Beam Milling

Florian Dell'Ova,[†] Konstantin Malchow,[†] Rémi Chassagnon,[†] Olivier Heintz,[†] Nicolas Pocholle,[†] Gérard Colas des Francs,[†] Erik Dujardin,[†,‡] and Alexandre Bouhelier[*,†]

†*Laboratoire Interdisciplinaire Carnot de Bourgogne, CNRS UMR 6303, Université de Bourgogne Franche-Comté, 9 Av. A. Savary, 21000 Dijon, France*

‡*CEMES CNRS UPR 8011 and University of Toulouse, 29 rue J. Marvig, 31055 Toulouse, France*

E-mail: alexandre.bouhelier@u-bourgogne.fr

Abstract

This paper explores the nonlinear photoluminescence emitted by Indium Tin Oxide (ITO) thin layers patterned by focused gallium ion beam milling. Using tightly focused near-infrared femtosecond pulsed laser excitation, a broad up-converted luminescence spanning the visible spectrum is detected. The intensity of the luminescence follows a non-monotonous relationship with milling doses and can be related to the modification of the ITO electronic band structure by the implantation of Ga ions. The shape and the power dependence of the spectrum share strong similarities with nonlinear photoluminescence arising from metals. The results are consistent with a nonlinear luminescence process originating from the radiative decay of photo-generated hot carriers. The ther-

mal coefficient relating the hot carrier temperature to the laser intensity is determined as a function of milling dose.

Keywords

Indium Tin Oxide; Patterned Film; Focused Ion Beam; Irradiation Dose, Femtosecond Pulses; Nonlinear Photoluminescence; Hot Electrons; Thermal Coefficient;

Introduction

Nonlinear photoluminescence (NPL) generated under intense pulse excitation is a material-specific response which may have different origin depending on the nature of the object under scrutiny. In semi-conductors, NPL is generally ascribed to a multi-photon absorption process populating an excited state and relaxing by radiative transitions in the band manifold. This sequence was observed in carbon nanotubes, graphene and graphene oxide, for instance.[1–3]

NPL has also been extensively discussed for metals with very different electronic band structures (e.g. Au, Ag, Al).[4–7] The general non-linear dependency to the laser intensity suggests that incident photons provide energy to promote electrons from a *d*-band to the conduction band. In particular, this dependency was measured nearly quadratic for Au, which has rooted the standard model based on two-photon interband transition.[8,9] However, a growing number of reported data cannot be fully cast within the framework of a multi-photon absorption process. In fact, the measured order of non-linearity may significantly vary with the specificity of the experiment: non-integer values[10] or large higher-orders[11,12] are often reported. Alternative mechanisms have recently been proposed to account for the up-converted broadband emission. They share one common feature which is the generation of an out-of-equilibrium electron gas swiftly produced after the absorption of the laser pulse.[13–15] In this framework, Lupton and co-workers have shown that the nonlinear exponent stems from an absorption process only at low laser intensity. At large power densities, the

nonlinearity is better described as arising from a radiating bath of electrons brought to very high temperatures.[16] Hot carriers generated upon laser irradiation in other systems such as gallium arsenide nanospheres[17] as well as in electrically-driven optical gap antennas[18,19] have recently confirmed that this incandescent emission is a fairly generic phenomenon. NPL is therefore a valuable observable to understand carrier relaxation in many-body systems and to explore novel photonic functionalities.[20]

Here, we discuss Indium Tin Oxide (ITO), a widely used transparent conductive oxide,[21] as yet another material sustaining a NPL response that is also satisfactorily understood in the framework of a radiating hot electron gas. ITO sustains a free-electron system with dispersive properties enabling controllable nonlinear properties notably in the context of epsilon-near-zero material[22,23] and ultrafast modulation.[24]

While NPL does not naturally occurs in pristine films of ITO, we reveal here that intense NPL emerges when ITO thin films undergo nanopatterning processes involving gallium focused ion beam milling. The NPL variations with the milling dose are correlated with a thorough structural and chemical surface analysis. Moreover, we carry out an exhaustive investigation of the NPL dependency on the laser intensity and polarization. Our findings unambiguously unveil the pivotal role of a heated electron gas in the origin of the observed NPL signal.

Results and discussion

Dose-dependent NPL generation

First, we examine the evolution of the NPL signal with the Ga^+ milling dose. The NPL reponse of the FIB-patterned ITO film is studied with the optical bench sketched in **Figure 1(b)**. The nonlinear nature and origin of the luminescence is discussed in Section . Figure 1(c) shows a confocal scan of the spectrally integrated NPL emitted by the FIB milled squares seen in Figure 1(a). The incident laser beam is linearly polarized along the

horizontal direction. The FIB-induced modification of the ITO thin film has a marked effect on the emission of which the salient features are clearly brought up in Figure 1(c). No detectable NPL is emitted from ITO areas that were not exposed to the ion beam. Initially, at the lowest dose (D = 6.3 pC cm^{-2}, top left corner of the array) the NPL barely stands out from the background but the amplitude of the nonlinear response increases with the milling dose up to a maximum that occurs at $D_\circ$ = 25.4 pC cm^{-2} (Figure 1(c), blue dot). In the first line of the array the NPL is homogeneously emitted from the 3 × 3 μm^2 exposed areas. Beyond $D_\circ$, the NPL signal collected from the interior of the milled areas steadily decreases back to the background count. At $D_\star$ = 44.4 pC cm^{-2} (Figure 1(c), blue star) the NPL is essentially detected from the edges of the structured area and no significant signal is recorded inside the milled square. Counter-intuitively, only the edges aligned with the polarization are generating a NPL signal that rapidly becomes extremely intense as the dose is further increased. The effect of the polarization will be discussed in Section .

The stricking non-monotonous evolution of the nonlinear signal with the dose involves several parameters. The FIB milling is likely to increase the ITO and glass substrate roughness. This could explain the increase of NPL in the upper line of the array in Figure 1(c). Indeed, the intensity of NPL emitted from Au films, are typically larger for rougher surfaces. The local field enhancement is usually credited for boosting the nonlinear response.[8] Yet local surface-plasmon assisted resonances are unlikely to occur in ITO for this wavelength range since the plasma frequency typically lies in the infrared.[25] Additionally, increasing the milling dose gradually reduces the thickness of the ITO layer and eventually over-etch it. Milling of the ITO layer proceed through a meshing that accounts for the gradual reduction of NPL beyond the dose $D_\circ$. Similarly, the absence of NPL from within the milled squares is consistent with the full removal of the material contributing to the NPL.

These hypotheses are confirmed by the plot displayed in **Figure 2**. Using high-resolution AFM imaging (data not shown), we measure the etched depth and estimate the surface roughness (root-mean square) that are displayed alongside the total integrated NPL signal

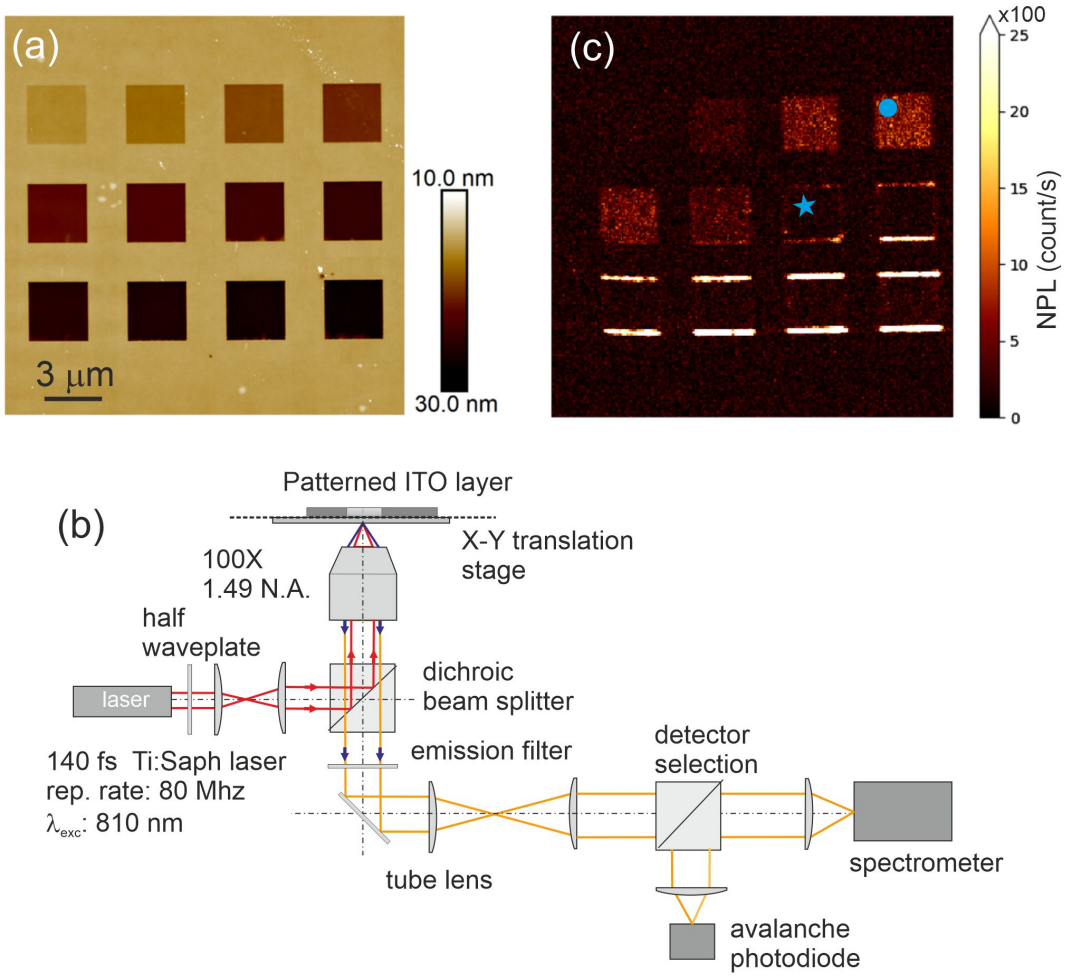

Figure 1: (a) Atomic force microscopy (AFM) image displaying the 4×3 array of 9 μm^2 areas focused-ion beam milled in a nominally 10 nm thick ITO layer. Each square is milled with a dose increment. (b) Schematics of the experimental bench. (c) Confocal NPL scan of the milled areas. The incident linear polarization is aligned horizontally. The blue dot marks the pattern showing the highest NPL amplitude inside the milled area. The blue star indicates the first pattern where the NPL emitted from the edges overcomes the signal from the interior area ($D_\star = 44.4$ pC cm^{-2})

measured within each element of the array and summed over a centered 4 μm^2 area. The roughness of the pristine layer is 0.18 nm and corresponds to $D = 0$ pC cm^{-2}. Clearly, the roughness of the milled squares increases with dose and is indeed correlated to a rise of the NPL up until $D_\circ$. $D_\circ$ corresponds to an etched depth of 11 nm that corresponds to the nominal thickness of ITO, so most of it is etched away and explains the onset of the vanishing NPL signal. For $D \geq D_\circ$, the ITO layer is completely removed and the ion beam mills the SiO_2 substrate. NPL is no longer generated from inside the milled where only a rough SiO_2 surface remains.

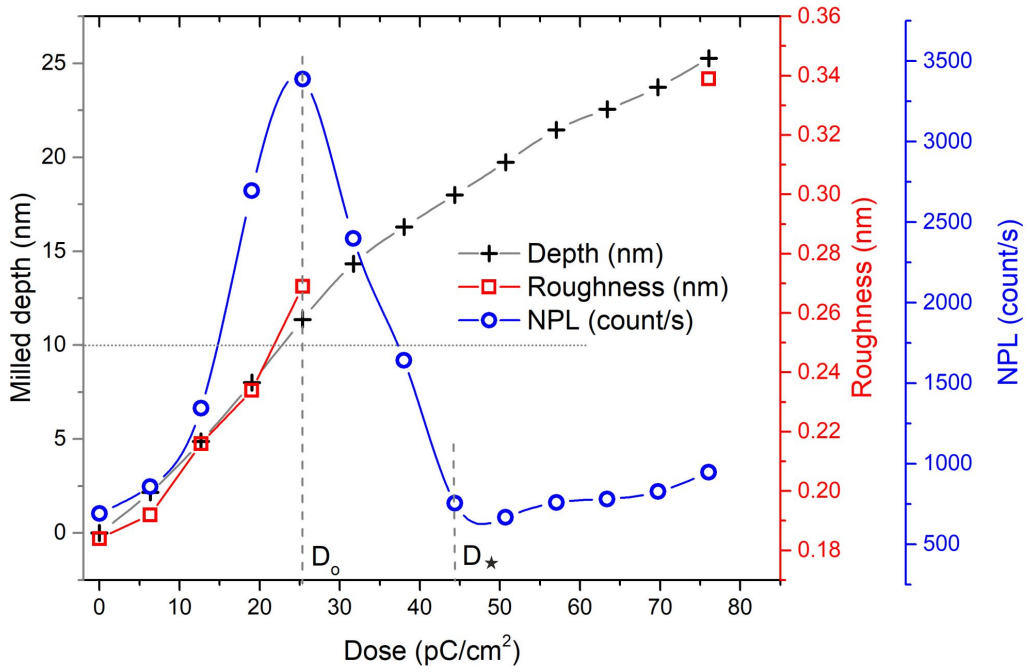

Figure 2: Evolution of the etched depth (black cross), roughness (red square) and NPL intensity (blue circle) as a function of the milling dose. The horizontal line materializes the nominal ITO thickness, the vertical one indicates the dose leading to the maximum NPL signal emitted by the interior of the milled area.

FIB-created surface roughness is concomitant to Ga^+ ion implantation. In order to deconvolute these effects, we have performed high fluence (27 MW cm^2) laser irradiation by repeatedly raster scanning a 3 $\times$ 3 μm^2 area of pristine ITO in order to reach the threshold of photo-modification. **Figure 3(a)** shows an AFM image of the optically-modified area featuring an additional thickness of 2.3 nm with a roughness of 0.21 nm confirming the

action of the pulsed laser. According to Figure 2, this roughness should give rise to an appreciable NPL signal. However, the confocal scan of the region displayed in Figure 3(b) features a homogeneous background count. Hence, a rough ITO film on SiO_2 is not sufficient to generate a NPL response, and suggests that the presence of gallium ions in the ITO/SiO_2 substrate is a necessary condition.

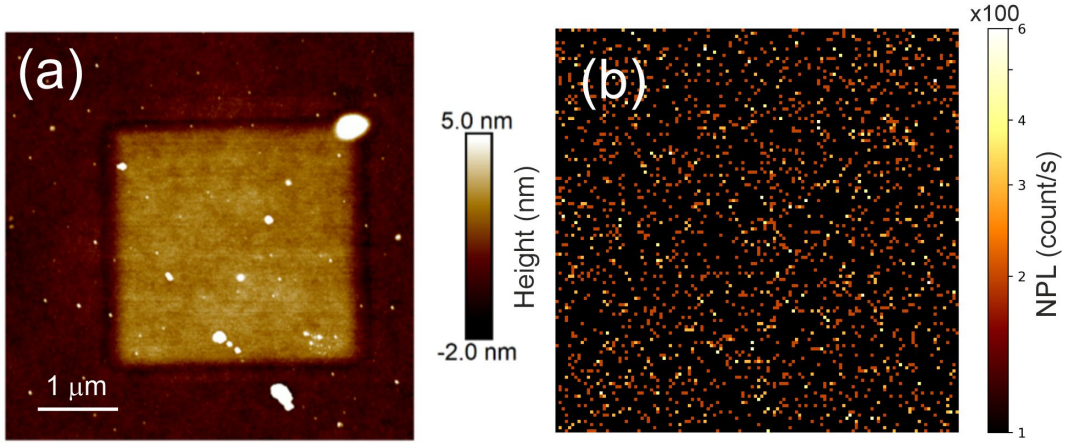

Figure 3: (a) AFM image of a 9 μm^2 area of bare ITO scanned repeatedly at the highest laser intensity. (b) Confocal map of the same area showing no detectable NPL response.

To address this point, we perform energy-dispersive X-ray (EDX) elemental mapping of the patterned array to obtain local chemical information. **Figure 4** shows energy-filtered maps of the distribution of Ga, O, In, and Si. The elemental map of Ga clearly indicates an increasing concentration of ions with the dose. This is concomitant to a reduction of In resulting from the sputtering of ITO. The O map is nearly constant because this elemental signature is present both in the ITO layer and in the SiO_2 substrate. The Si signal increases with the dose, which confirms that the SiO_2 sub-surface is probed more efficiently as the etching proceeds. Figure 4 unambiguously demonstrates that Ga ions or Ga clusters alone do not produce any nonlinear photoluminescence on their own because the elemental map diverges from the NPL map when $D > D_\circ$. Nonetheless, Ga atoms implanted during the etching process are likely to act as doping impurities of the amorphous matrix of ITO. For the square $D_\star$ the atomic percentage of Ga reaches 1.45 % (Figure 4) in the probed volume.

Interestingly, the doping of indium oxide by gallium atoms at a few percent level has been linked to an increase of electrical conductivity.[26] More specifically, amorphous Ga:In_2O_3 features a distinctive density of states with a closure of the band-gap and the transition to a metal-like material.[27,28] The distortion of the ITO electronic band structure by Ga^+ may reasonably explain the appearance of the NPL signal in beam-exposed areas.

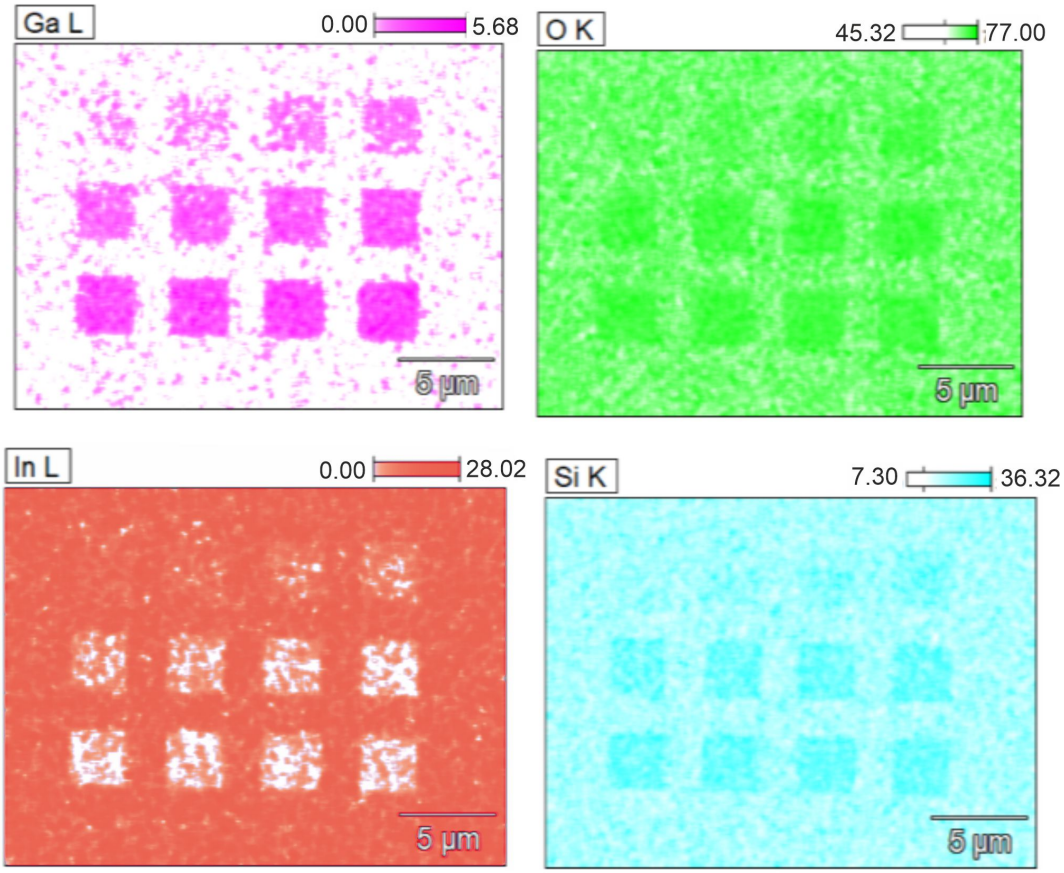

Figure 4: Energy-dispersive X-ray maps of relevant materials (Ga, In, Si and O). The color scale is in atomic percentage.

Effect of the edges and their sensitivity to the polarization

In this section examine the intense NPL production from the edges of the milled areas revealed in Figure 1 for $D \geq D_\star$. The NPL signal is only observed for edges aligned along the polarization direction. In contrast, the NPL emitted by metal step edges is maximized by an

excitation polarized perpendicularly to the step that favors the localisation and enhancement of the local electric field.[29] **Figure 5(a)** depicts an AFM image of a wheel-like milled structure specifically realized to study the effect of polarization. The wheel consists of rectangular trenches radially distributed with a 30° increment. The dose used here exceeds $D_\star$ to fully etch the ITO. Figure 5(b) to (d) show NPL maps taken by raster scanning the wheel in the focus of the beam with three different orientations of the incident polarization, as indicated by the double arrows. The confocal scans unambiguously demonstrate that a component of polarization must be aligned with an edge in order to produce a NPL response. No signal is coming from the edges of the trenches orthogonal to the polarization. The extinction is not total at 45° because the dichroic beam splitter reduces the degree of polarization for this incident polarization.

In the absence of moment transfer provided by the physical interface when the polarization is aligned with an edge, we conclude that the localisation and the enhancement of the electric field is not a prerequisite for producing a high NPL response on patterned ITO. Interestingly, we also find that the emitted light is partially polarized along the edge. By placing an analyzer in front of the APD, we determine the degree of polarization:

$$V = \frac{I_{NPL}^{\max} - I_{NPL}^{\min}}{I_{NPL}^{\max} + I_{NPL}^{\min}} = 0.77 \tag{1}$$

where $I_{NPL}^{\max}$ and $I_{NPL}^{\min}$ are the NPL intensity extrema measured by rotating the analyzer. For isotropic semi-conductors, the degree of polarization of a luminescent material can generally be related to the presence of strain or dislocations.[30] It is not clear if this mechanism can be applied to the nonlinear signal discussed here, but there is a correlation between the NPL and the local morphology of patterned film. This correlation is materialized in **Figure 6** showing height and NPL cross-sections extracted from trench '9' and measured for both transverse and longitudinal directions. The intense NPL signal coincides with a ∼1 nm tall hillock located at the boundary of the trench which signals a morphological change of the ITO. Indeed, during the process of raster scanning the ion beam, extra etching occurs

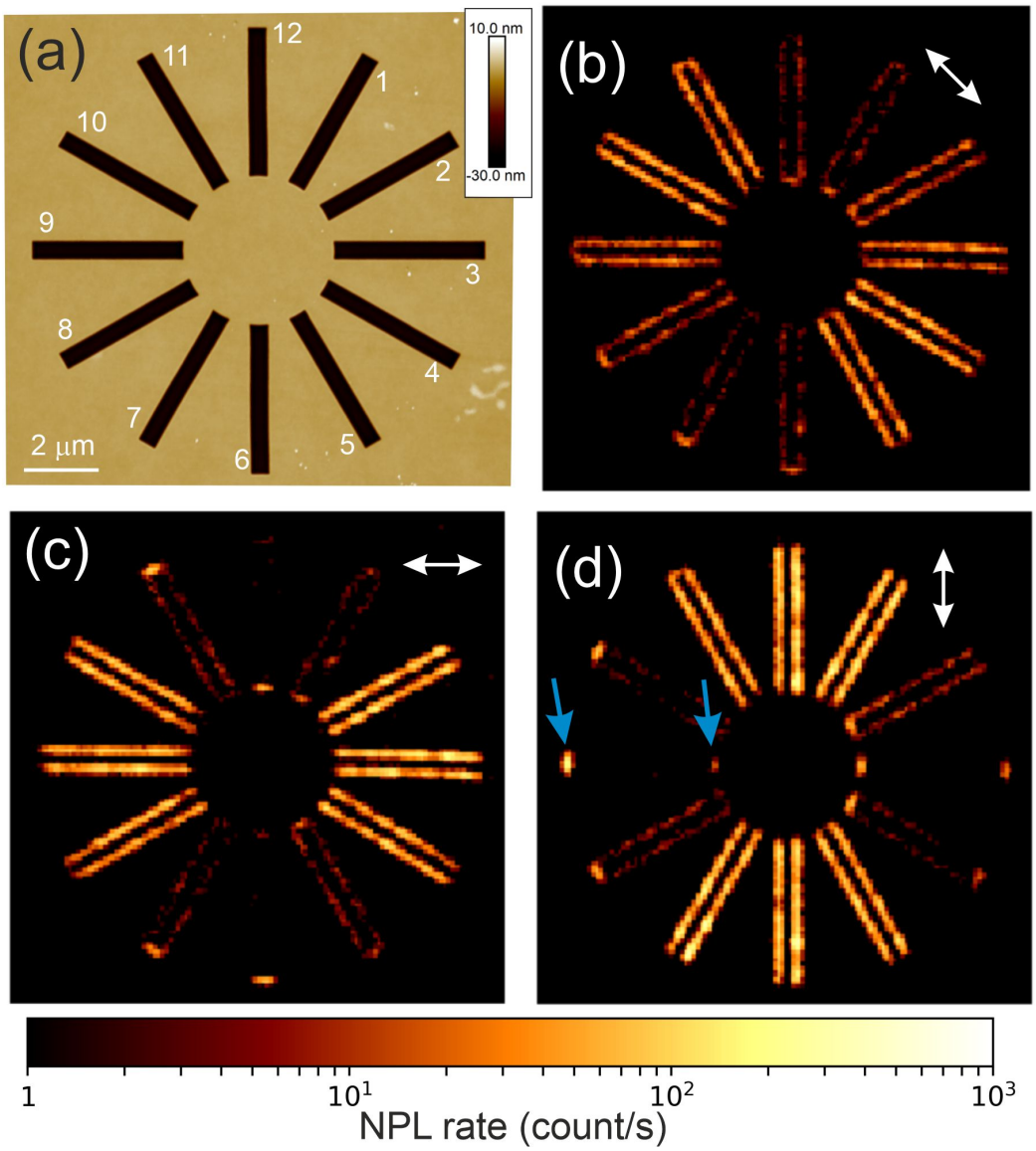

Figure 5: (a) Atomic force image displaying the circularly symmetric pattern fully etched in the ITO. Corresponding NPL maps taken with an incident polarization angle of 45° (b), 0° (c) and 90° (d) (white double arrows). The blue arrows mark the effect of the ion beam milling strategy (see text for details). The intensity is in logarithmic scale to help visualizing even the dimmest regions.

at the beginning of the scanned trajectory due to a finite lag of the beam stirring plates from the parking position, and conversely, a lesser etching occurs at the end of the scanning trajectory because of the reduced proximity effect from the adjacent pixels. In our case, the FIB rastering strategy is linked to the rectangular patterns. The beam is fast scanned along lines parallel to the small axis, stepping line by line along the long axis in the inward (resp. outward) direction for trenches '12' to '5' (resp. '6' to '11'). The complete etch is performed in multiple raster scans and we consistently observe a symmetric deformation along the length of the trench as shown in the height profile of Figure 6(a). If we associate the structural damaged indicated by the bulge with a corresponding amount of beam exposure and so implanted gallium ions, the AFM profiles in Figure 6(a) suggests a uniform gallium implantation density along both long edges, a higher (resp. smaller) one for the outmost (resp. innermost) short edge of trench '9'. This relative distribution is accurately echoed in the NPL intensity along the corresponding edges.

If now, we flip the excitation polarization to 90° as in Figure 5(d), we recognize that the NPL is emitted by the short edges of trenches '3' and '9' and also the long edges of trenches '6' and '12', which are aligned with the flipped incident polarization. Importantly, an asymmetric response of the short edges is highlighted by the blues arrows in Figure 5(d) and are perfectly in line with the corresponding bulges in Figure 6(b). A higher (resp. lower) intensity is associated with a larger (resp. smaller) bulge. In Figure 6(b), the intensity of the NPL is indeed much lower at the side corresponding to the start of the milling pattern where a local over-etch of the glass substrate is measured, shortly before the coordinate 5 μm. On the contrary, the brightest nonlinear signal is located at the edge formed by the end of the milling pattern where the ion implantation leads to a hillock (coordinate 1 μm).

On the origin of the nonlinear photoluminescence

We now carry an in-depth analysis of the laser dependence on the NPL response to quantify its nonlinear character. To this aim, we systematically record the emission spectra from a

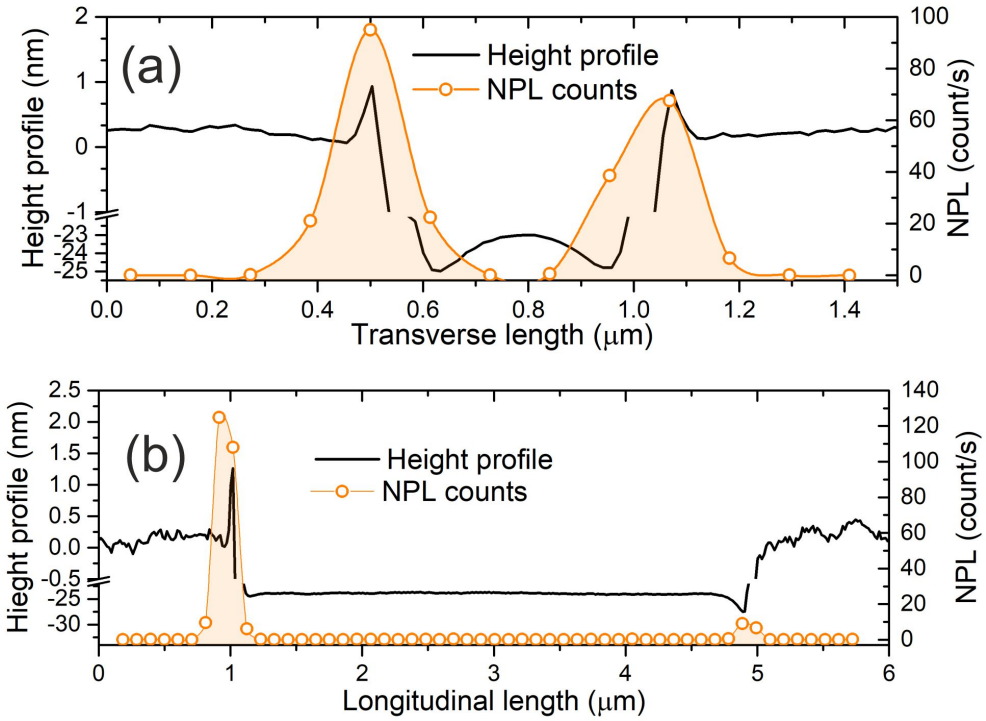

Figure 6: Height and NPL profiles extracted from (a) the transverse and (b) longitudinal axis of the left horizontal branch of trench '9' in Figure 5(a). The profiles are average over the entire width and length of the branch. NPL profile in (a) (resp. (b)) is extracted from NPL map Figure 5(c) (resp. (d)).

series of etched squares for sweeping incident intensities of the laser. **Figure 7(a)** shows representative spectra emitted by the circle-labelled square in Figure 1(c) for the lowest, intermediate and highest incident intensities of the sweep. We ensured that the maximum intensity used during the experiment is below the irreversible damage threshold. We also checked that the confocal scans of the probed area taken before and after conducting the intensity sweeps remain similar.

All the spectra share the same overall shape. They are corrected to take into account the spectral efficiency of the detection (transmission of the objective and filters, CCD quantum efficiency, grating efficiency). The NPL monotonously decays toward short wavelengths. In contrast to NPL emitted from metallic nano-objects,[31] no resonance or shoulder shaping the emission spectrum is observed here. This absence of well-defined features in the spectra confirms that a local field enhancement is not a prerequisite to explain NPL generated from patterned ITO.

In the following, we assume that NPL stems from an out-of-equilibrium electronic distribution swiftly radiatively relaxing after the absorption of the laser pulse, a mechanism already proposed to account for metal nonlinear photoluminescence.[6,15,16] Since hot carriers are also generated in ITO after pulsed excitation and are essential to explain coherent higher-order ITO nonlinearities,[23] we apply here the same methodology used to characterize metal NPL.

The absorption of a femtosecond laser pulse by a conductor leads to a transient temperature increase of the electron gas quickly relaxing to the vibrational degrees of freedom. When these hot carriers are colliding with the physical boundary of the reservoir (e.g. roughness, edges, etc.), additional radiative relaxation channels are opening[32] that are reflecting the energy distribution of the electron gas. We thus assume that the NPL spectrum is associated to a black-body radiation by the spontaneous decay of the hot electrons. The electronic temperature T_e can be estimated by fitting the emission spectrum with Planck's law:

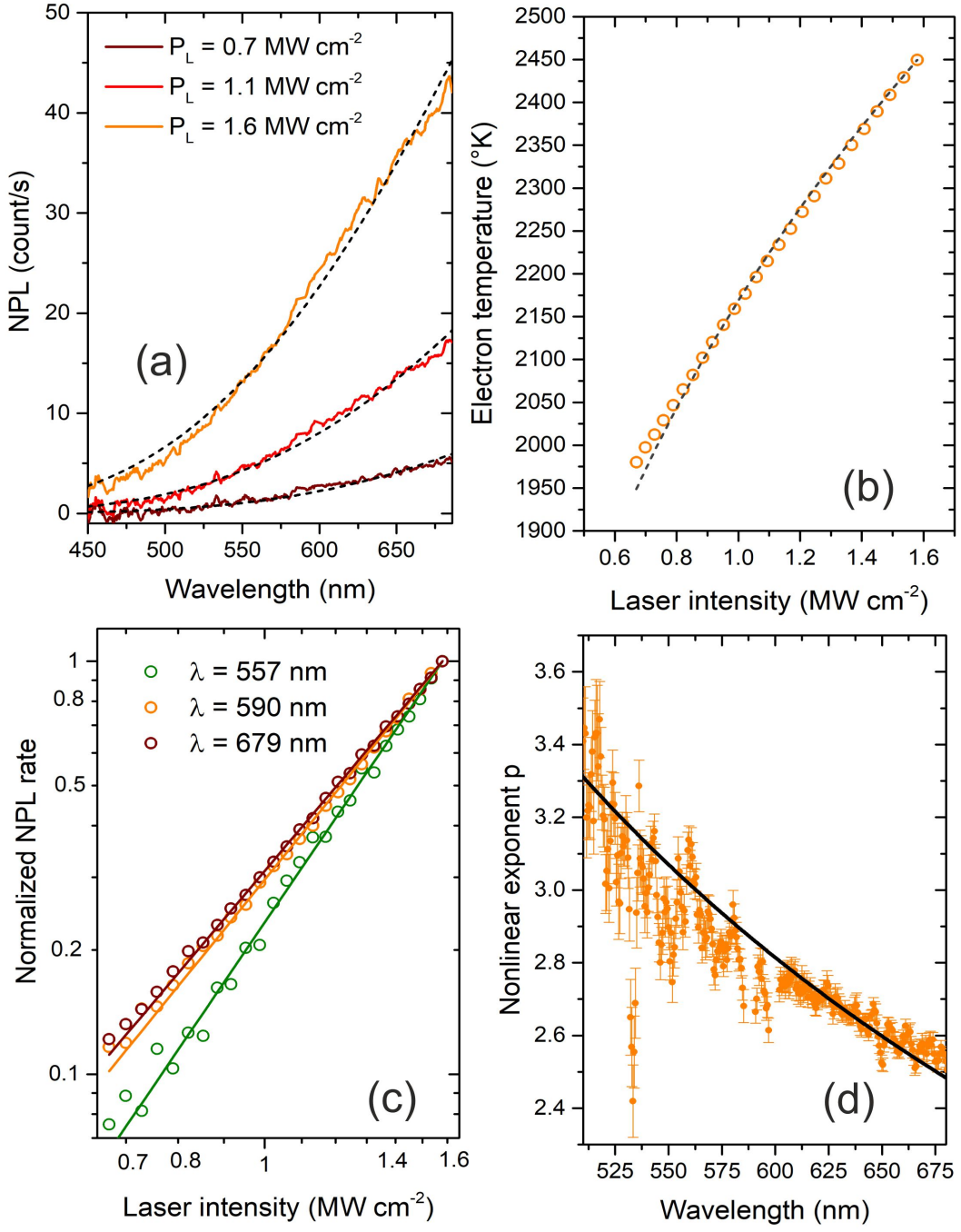

Figure 7: (a) Typical NPL spectra emitted by FIB-milled ITO acquired at minimum, intermediate and maximum laser intensities. The dashed lines are fit using a thermal emission model. The spectra are corrected by the transmittance of the optical path inferred from suppliers' specifications. (b) Dependence of the electron temperature T_e with the laser intensity. T_e are deduced from the fits in (a). The dashed line is a power fit yielding the thermal coefficient a. (c) Variation of NPL amplitude taken at three wavelengths. The solid lines are power law fits used to infer the nonlinearity exponent p. (d) Dispersion of the nonlinearity exponent p. The solid line is a fit using the thermal model of Equation 3. The spurious data set at around 530 nm is stemming from damaged pixels on the CCD detector.

$$I_{NPL}(\lambda, T_{\mathrm{e}}) = \frac{C}{\lambda^4 \left(\exp \frac{hc}{\lambda k_B T_{\mathrm{e}}} - 1\right)} \tag{2}$$

where $I_{NPL}(\lambda, T_{\mathrm{e}})$ is the amplitude of the NPL spectrum at a given wavelength λ and T_{e}, h is the Planck's constant, k_B is the Boltzmann's constant and c is the speed of light in vacuum. In the absence of resonances in the spectra of Figure 7(a), C is a constant prefactor and is considered as a free parameter. The dashed lines in Figure 7(a) are fits of the experimental spectra using Equation 2. C is determined from the spectrum taken at the highest laser intensity and used subsequently to fit the remaining data set. Equation 2 reasonably reproduces the measured spectral shapes and we can therefore readily extract T_{e} for each laser intensity P_{L}. This is shown in Figure 7(b). Understandably, the electron temperature depends on the laser intensity $T_e^a \propto P_{\mathrm{L}}$ as a consequence of the amount of optical power absorbed by the material. a is a thermal coefficient and, in the limit of low temperature, is equal to 2.[33] We determine the thermal coefficient to be $a = 3.76 \pm 0.06$ by fitting the data with a power law.

Thermal coefficients significantly diverging from the low temperature value have already been reported for NPL emitted from metal objects.[6,16] The measured value of a for ITO can be qualitatively explained by the same line of argumentation. In essence, following the absorption of the 140 fs laser pulse, the electron sub-system is brought at elevated T_{e} which results in a significant change in the electronic population distribution in the conduction band. The electron heat capacity C_{e} can no longer be considered as a linear function of T_{e}.[34,35] A more quantitative description is a difficult task at this stage since details of the band structure and the density of states are required to evaluate precisely $C_{\mathrm{e}}(T_{\mathrm{e}})$. We do not know how these parameters are modified by the milling process and the gallium implantation, but the large a coefficient is an indirect manifestation of a modified ITO band structure. We perform a similar analysis on the other etched squares emitting a measurable NPL signal, as well as on one of the edges rendering a strong response ($D = 57.0$ pC cm^{-2})

and a reference Au film. The results are reported in **Table 1**. We observe a steady decrease of the thermal coefficient a with dose D for NPL emitted inside the etched areas. It is clear that larger milling doses leads to an increased modification of electronic structure of pristine ITO. In light of the above discussion, it is reasonable to state that D is affecting C_{e} and by consequence the thermal coefficient a. For doses comprised between D_o and $D_\star$ the NPL intensity is so dim that spectra could not be recorded with an acceptable signal-to-noise ratio. Interestingly, for these intermediate doses, the damage threshold was extremely low suggesting that the ITO film was quite unstable and probably composed of scattered nanoparticles very sensitive to light-induced degradation.

Table 1: Values of the thermal parameter a as a function of the nominal FIB milling dose.

Dose D (pC cm^{-2})	Thermal coefficient a
12.7	4.9±0.2
19.0	4.2±0.1
25.4 (D_o)	3.76±0.06
57.0 (edge)	4.05±0.07
Au	3.30±0.05

Let us now come back to the nonlinearity of the NPL with laser intensity. We shall see in the following the congruity of the data at supporting the contributing radiative decay of a hot electron gas as the origin of the NPL. In Figure 7(c), we plot the evolution of the NPL signal with laser intensity at three representative wavelengths. The plots are normalized to their respective maxima. The linear trends in this double logarithmic representation clearly evidence the amplitude dependence $I_{NPL} \propto P_{\mathrm{L}}^{p}$. We note that the slopes, providing the nonlinearity exponent p, are evolving with wavelength. Here too, this behavior bears strong similarities with NPL emitted by noble metals for large laser intensities.[6,15] In Figure 7(d), we gather the inferred nonlinear exponent p for all meaningful wavelengths and fit the data with its dependence expected from electron gas luminescence:[15]

$$p(\lambda, T_{\mathrm{e}}^{*}) = \frac{hc}{\lambda k_B T_{\mathrm{e}}^{*} a} \tag{3}$$

where T_e^* is the mean electronic temperature deduced from the laser intensity sweep. The value of $a = 3.76$ is obtained from Figure 7(b) and all other parameters are fixed, so that the adjustment of Equation 3 to the data depends solely on the T_e^*. The fit shown as a solid line in Figure 7(d) gives T_e^*= 2264 K, which lies in the middle of the T_e range extracted from Planck's fit in Figure 7(b).

We extend the nonlinear exponent analysis to the other measurable ITO areas etched with the doses of Table 1 and the reference gold film. The results of $p(\lambda)$ are displayed in **Figure 8**. For the lowest dose giving rise to a NPL response (D = 12.7 pC cm^{-2}) p is constant at 2.1 close to the constant power law exponent $p = 2$ reported by Roloff et al.[16] for Au nanoparticles irradiated under a regime of low laser intensities. The authors attributed the constant exponent to the signature of a two-photon absorption process. Here, the constant and quasi quadratic behaviour is observed for the same laser intensity as the non-linear and non-quadratic behaviour associated to higher irradiation doses. Instead, we claim that gallium implantation at D = 12.7 pC cm^{-2} has not fully closed the ITO band gap and an incoherent absorption of two photons is responsible for the photoluminescence. For the higher doses displayed in Figure 8, the nonlinear exponent is dependent on the wavelength reflecting the telltale signature of thermal radiation. The experimental data can be reasonably fitted by Equation 3 with the value of aT_e^* left as a free parameter. We deduce the mean electronic temperature T_e^* by using a values reported in Table 1. The inferred T_e^* for all doses and material fall within the range of electronic temperature extracted from fitting the laser intensity dependent spectra with a blackbody response (Equation 2). The consistency of the data set and the resemblance to the better characterized response of metal nanostructures confirm our stand point that NPL emitted by patterned ITO is the manifestation of a radiatively decaying hot electron gas.

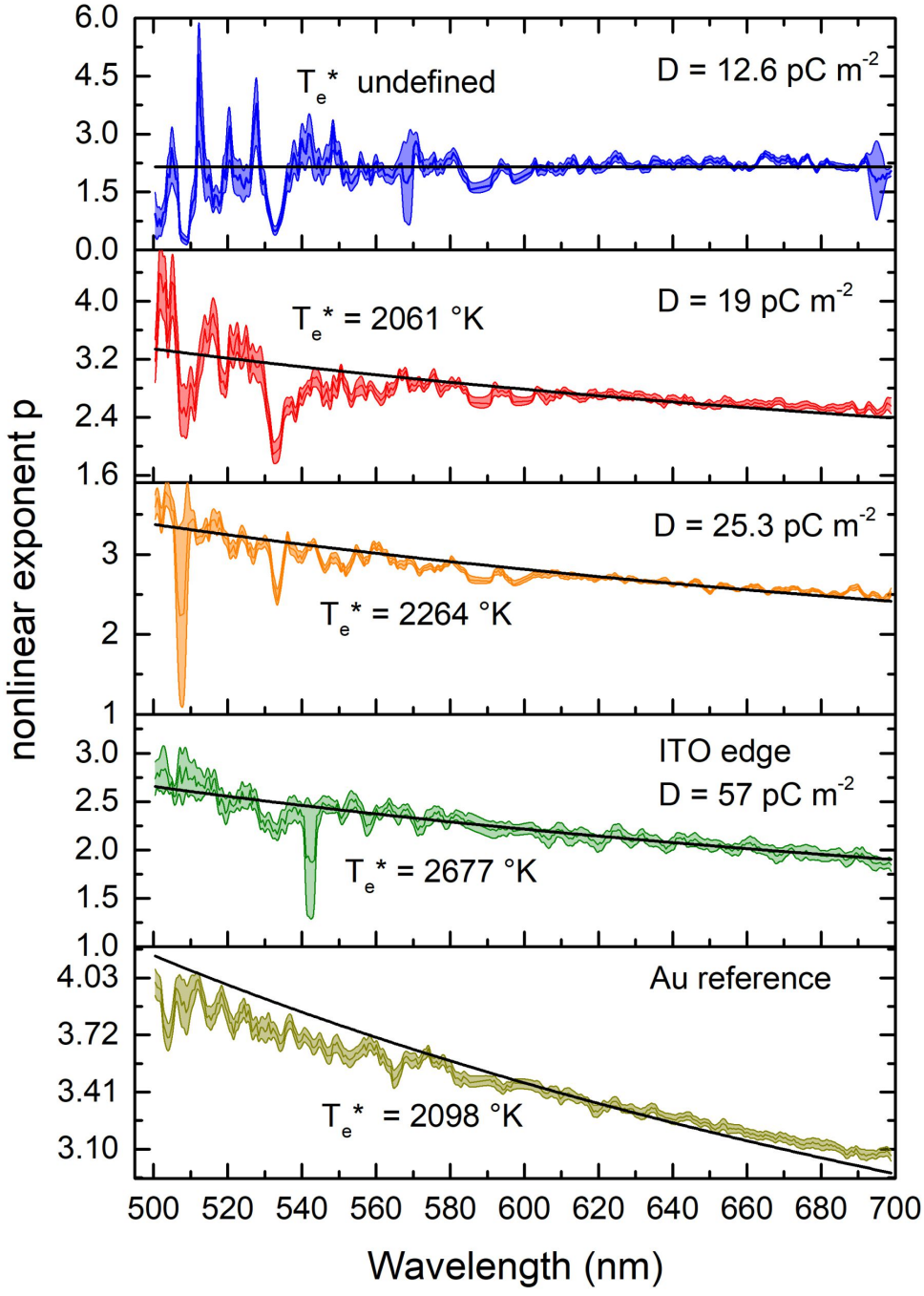

Figure 8: Dispersion of the nonlinearity exponent p from NPL emitted by areas milled at different ion doses. The two bottom most panels show the data for a bright ITO edge and a Au film for reference. The solid lines are fit according to Equation 3. The inferred mean electronic temperature T_e^* is indicated in each graphs.

Conclusion

Despite being widely used in industry, understanding and encompassing the variety of electrical and optical properties of ITO remains a vivid research topic. In this paper, we have revealed an undocumented behavior of ITO that has undergone ion beam milling. When excited by a near infrared focused femtosecond laser, on-beam modified ITO emits an up-converted photoluminescence signal covering a large spectral range in the visible domain. A series of indicators such as the material chemical composition, dependence of the nonlinear response on the etching parameters and polarization of the incident laser beam suggests that the nonlinear photolumines- cence is activated by a modification of the ITO band structure by Ga dopant implanted during the milling process. In this respect, it would be valuable to locally probe quantitatively the electronic structure of the modified ITO layer. Importantly, the spectral content and its nonlinear evolution with the laser intensity are fully accounted for by considering the radiative decay of out-of-equilibrium hot electron gas formed upon absorption of the laser pulse. This description bears strong similarity with non-linear photoluminescence emitted by metal objects. However, we also reveal ITO-specific properties. The response to the incident polarization is opposite to that observed with metal. We also found that the emitted signal is partially polarized and that can probably due to a local strain introduced by the implanted Ga ions. Finally, our data establish that a field enhancement is not required to trigger the nonlinear response in patterned ITO whereas this is a salient feature in plasmonic objects.

Experimental Section

ITO substrate preparation

Glass coverslips coated with a nominal 10 nm thick ITO layer are purchased from Diamond Coatings Ltd (West Midlands, UK). The layer has a resistivity of approximately 1 $k\Omega$ /square

and a transmission over 80 % in the 450 to 700 nm wavelength range as given by the supplier. The chemical content of the ITO coating is measured by photoelelectron spectroscopy (XPS) using two different sources $K\alpha$ Al (1486.7 eV) and $K\alpha$ Cr (5414.8 eV). The respective positions of the $3d_{5/2}$ levels of indium (444.3 eV) and tin (486.1 eV) reveal the presence of Sn^{4+} and In^{3+} identified[36] as SnO_2 and In_2O_3 in element percentage : O (70 %at), In (27 %at) and Sn (3 %at). The XPS depth profile obtained under Ar sputtering confirms the homogeneity of the ITO layer and its nominal 10 nm thickness using SiO_2 etching rate as reference.

Patterned specimens consist of 4×3 square arrays milled with a focused gallium ion beam (FIB) on a FEI Helios 660i dual FIB-SEM microscope. The parameters used for etching are a nominal probe current of 7 pA and an accelerating voltage of 30 kV with an incremental dose D ranging from 6.3 to 76.1 pC cm^{-2} with a constant step of 6.34 pC cm^{-2}. Each square covers an area of 9 μm^2 and are 2 μm spaced from each others to avoid any proximity effects.

Nonlinear photoluminescence microscopy

The optical bench used to excite and detect the NPL response of the FIB-patterned ITO films is an inverted confocal microscope. The microscope is equipped with a high numerical aperture objective lens (N.A. 1.49), which focuses a pulsed Ti:Saph laser beam onto a diffraction-limited spot ($\sim$ 270 nm full-width at half maximum). The laser delivers 140 fs pulses with repetition rate of 80 MHz and is tuned at a wavelength of 810 nm. The sample is placed on a x, y piezoelectric scanner and is excited with an epi-illumination configuration. The average laser intensity at the focal spot is estimated at 920 kW cm^{-2}. The up-converted NPL signal is spectrally separated from the laser wavelength by a combination of a dichroic beam splitter and a bandpass emission filter. The transmitted light emitted in the 450 to 700 nm wavelength range is detected either by an avalanche photodiode to reconstruct a NPL map of the sample or by a spectrometer to analyse the spectral content. The polarization and the laser power incident on the sample are fully controlled.

Acknowledgement

This work has been partially funded by the French Agence Nationale de la Recherche (ANR-20-CE24-0001 DALHAI and ISITE-BFC ANR-15-IDEX-0003), the EIPHI Graduate School (ANR-17-EURE-0002), and the European Union through the PO FEDER-FSE Bourgogne 2014/2020 programs. Device characterization was performed at the technological platforms SMARTLIGHT and ARCEN Carnot with the support of the French Agence Nationale de la Recherche under program Investment for the Future (ANR-21-ESRE-0040), the Région de Bourgogne Franche-Comté, the CNRS and the French Renatech+ network.

References

References

(1) Brennan, M. E.; Coleman, J. N.; Drury, A.; Lahr, B.; Kobayashi, T.; Blau, W. J. Nonlinear photoluminescence from van Hove singularities in multiwalled carbon nanotubes. *Opt. Lett.* **2003**, *28*, 266–268.

(2) Liu, W.-T.; Wu, S. W.; Schuck, P. J.; Salmeron, M.; Shen, Y. R.; Wang, F. Nonlinear broadband photoluminescence of graphene induced by femtosecond laser irradiation. *Phys. Rev. B* **2010**, *82*, 081408.

(3) Senyuk, B.; Behabtu, N.; Pacheco, B. G.; Lee, T.; Ceriotti, G.; Tour, J. M.; Pasquali, M.; Smalyukh, I. I. Nonlinear Photoluminescence Imaging of Isotropic and Liquid Crystalline Dispersions of Graphene Oxide. *ACS Nano* **2012**, *6*, 8060–8066.

(4) Klemm, P.; Haug, T.; Bange, S.; Lupton, J. Time-Domain Interferometry of Surface Plasmons at Nonlinear Continuum Hot Spots in Films of Silver Nanoparticles. *Phys. Rev. Lett.* **2014**, *113*, 266805.

(5) Wiecha, P. R.; Mennemanteuil, M.-M.; Khlopin, D.; Martin, J.; Arbouet, A.;

Gérard, D.; Bouhelier, A.; Plain, J.; Cuche, A. Local field enhancement and thermoplasmonics in multimodal aluminum structures. *Phys. Rev. B* **2017**, *96*, 035440.

(6) Malchow, K.; Bouhelier, A. Photon bunching of the nonlinear photoluminescence emitted by plasmonics metals. *J. Opt. Soc. Am. B* **2021**, *38*, 576–583.

(7) R. Lässer, N. S.; Benbow, R. L. Empirical and calculations of the optical properties of d-band metals. I. Cu, Ag and Au. *Phys. Rev. B* **1981**, *24*, 1895.

(8) Boyd, G. T.; Yu, Z. H.; Shen, Y. R. Photoinduced luminescence from the noble metals and its enhancement on roughned surface. *Phys. Rev. B* **1986**, *33*, 7923–7936.

(9) Imura, K.; Nagahara, T.; Okamoto, H. Near-Field Two-Photon-Induced Photoluminescence from Single Gold Nanorods and Imaging of Plasmon Modes. *J. Phys. Chem. B* **2005**, *109*, 13214–13220.

(10) Chen, J.; Krasavin, A.; Ginzburg, P.; Zayats, A. V.; Pullerits, T.; Karki, K. J. Evidence of High-Order Nonlinearities in Supercontinuum White-Light Generation from a Gold Nanofilm. *ACS Phot.* **2018**, *5*, 1927–1932.

(11) Mühlschlegel, P.; Eisler, H.-J.; Martin, O. J. F.; Hecht, B.; Pohl, D. W. Resonant Optical Antennas. *Science* **2005**, *308*, 1607–1609.

(12) Méjard, R.; Verdy, A.; Petit, M.; Bouhelier, A.; Cluzel, B.; Demichel, O. Energy-Resolved Hot-Carrier Relaxation Dynamics in Monocrystalline Plasmonic Nanoantennas. *ACS Phot.* **2016**, *3*, 1482–1488.

(13) Huang, J.; Wang, W.; Murphy, C. J.; Cahill, D. G. Resonant secondary light emission from plasmonic Au nanostructures at high electron temperatures created by pulsed-laser excitation. *Proc. Nat. Acad. Sci.* **2014**, *111*, 906–911.

(14) Wang, J.; Baudrion, A.-L.; Béal, J.; Horneber, A.; Tang, F.; Butet, J.; Martin, O. J. F.; Meixner, A. J.; Adam, P.-M.; Zhang, D. Hot carrier-mediated avalanche multi-

photon photoluminescence from coupled Au-Al nanoantennas. *J. Chem. Phys.* **2021**, *154*, 074701.

(15) Haug, T.; Klemm, P.; Bange, S.; Lupton, J. M. Hot-Electron Intraband Luminescence from Single Hot Spots in Noble-Metal Nanoparticle Films. *Phys. Rev. Lett.* **2015**, *115*, 067403.

(16) Roloff, L.; Klemm, P.; Gronwald, I.; Huber, R.; Lupton, J. M.; Bange, S. Light Emission from Gold Nanoparticles under Ultrafast Near-Infrared Excitation: Thermal Radiation, Inelastic Light Scattering, or Multiphoton Luminescence? *Nano Lett.* **2017**, *17*, 7914–7919.

(17) Xiang, J.; Jiang, S.; Chen, J.; Li, J.; Dai, Q.; Zhang, C.; Xu, Y.; Tie, S.; Lan, S. Hot-Electron Intraband Luminescence from GaAs Nanospheres Mediated by Magnetic Dipole Resonances. *Nano Lett.* **2017**, *17*, 4853–4859.

(18) Buret, M.; Uskov, A. V.; Dellinger, J.; Cazier, N.; Mennemanteuil, M.-M.; Berthelot, J.; Smetanin, I. V.; Protsenko, I. E.; Colas-des-Francs, G.; Bouhelier, A. Spontaneous Hot-Electron Light Emission from Electron-Fed Optical Antennas. *Nano Lett.* **2015**, *15*, 5811–5818.

(19) Zhu, Y.; Cui, L.; Natelson, D. Hot-carrier enhanced light emission: The origin of above-threshold photons from electrically driven plasmonic tunnel junctions. *J. Appl. Phys.* **2020**, *128*, 233105.

(20) Kumar, U.; Viarbitskaya, S.; Cuche, A.; Girard, C.; Bolisetty, S.; Mezzenga, R.; Colas des Francs, G.; Bouhelier, A.; Dujardin, E. Designing Plasmonic Eigenstates for Optical Signal Transmission in Planar Channel Devices. *ACS Phot.* **2018**, *5*, 2328–2335.

(21) Dalapati, G. K.; Sharma, H.; Guchhait, A.; Chakrabarty, N.;, Bamola P.; Liu, Q.; Saianand, G.;Sai Krishna, A. M.; Mukhopadhyay, S.; Dey, A.; Wong, T. K. S.; Zhuk, S.;

and Ghosh, S.; Chakrabortty, S.; Mahata, C.; Biring, S.; Kumar, A.; Ribeiro, C. S.; Ramakrishna, S.; Chakraborty, A. K.; Krishnamurthy, S.; Sonar, P.; Sharma, M. Tin oxide for optoelectronic, photovoltaic and energy storage devices: a review. *J. Mater. Chem. A* **2021**, *9*, 16621–16684.

(22) Zahirul Alam, M.; De Leon, I.; Boyd, R. W. Large optical nonlinearity of indium tin oxide in its epsilon-near-zero region. *Science* **2016**, *352*, 795–797.

(23) Rodríguez-Suné, L.; Scalora, M.; Johnson, A. S.; Cojocaru, C.; Akozbek, N.; Coppens, Z. J.; Perez-Salinas, D.; Wall, S.; Trull, J. Study of second and third harmonic generation from an indium tin oxide nanolayer: Influence of nonlocal effects and hot electrons. *APL Photonics* **2020**, *5*, 010801.

(24) Guo, P.; Schaller, R. D.; Ocola, L. E.; Diroll, B. T.; Ketterson, J. B.; Chang, R. P. H. Large optical nonlinearity of ITO nanorods for sub-picosecond all-optical modulation of the full-visible spectrum. *Nat. Commun.* **2016**, *7*, 12892.

(25) Brewer, S. H.; Franzen, S. Indium Tin Oxide Plasma Frequency Dependence on Sheet Resistance and Surface Adlayers Determined by Reflectance FTIR Spectroscopy. *J. Phys. Chem. B* **2002**, *106*, 12986–12992.

(26) Liu, Y.; Xu, W.; Liu, D.-B.; Yu, M.; Lin, Y.-H.; Nan, C.-W. Enhanced thermoelectric properties of Ga-doped In2O3 ceramics via synergistic band gap engineering and phonon suppression. *Phys. Chem. Chem. Phys.* **2015**, *17*, 11229–11233.

(27) Ramzan, M.; Kaewmaraya, T.; Ahuja, R. Molecular dynamics study of amorphous Ga-doped In2O3: A promising material for phase change memory devices. *Appl. Phys. Lett.* **2013**, *103*, 072113.

(28) Cocemasov, A. I.; Brinzari, V. I.; Nika, D. L. Energetic, structural and electronic features of Sn-, Ga-, O-based defect complexes in cubic In2O3. *J. Phys.: Condens. Matter* **2020**, *32*, 225703.

(29) Beermann, J.; Novikov, S. M.; Holmgaard, T.; Eriksen, R. L.; Albrektsen, O.; Pedersen, K.; Bozhevolnyi, S. I. Polarization-resolved two-photon luminescence microscopy of V-groove arrays. *Opt. Express* **2012**, *20*, 654–662.

(30) Cassidy, D. T.; Lam, S. K. K.; Lakshmi, B.; Bruce, D. M. Strain mapping by measurement of the degree of polarization of photoluminescence. *Appl. Opt.* **2004**, *43*, 1811–1818.

(31) Bouhelier, A.; Bachelot, R.; Lerondel, G.; Kostcheev, S.; Royer, P.; Wiederrecht, G. P. Surface Plasmon Characteristics of Tunable Photoluminescence in Single Gold Nanorods. *Phys. Rev. Lett.* **2005**, *95*, 267405.

(32) Uskov, A. V.; Khurgin, J. B.; Buret, M.; Bouhelier, A.; Smetanin, I. V.; Protsenko, I. E. Biased Nanoscale Contact as Active Element for Electrically Driven Plasmonic Nanoantenna. *ACS Phot.* **2017**, *4*, 1501–1505.

(33) Gamaly, E. *Femtosecond Laser-Matter Interaction: Theory, Experiments and Applications*; Pan Stanford Publishing Pte. Ltd: Singapore, 2011.

(34) Lin, Z.; Zhigilei, L. V.; Celli, V. Electron-phonon coupling and electron heat capacity of metals under conditions of strong electron-phonon nonequilibrium. *Phys. Rev. B* **2008**, *77*, 075133.

(35) Hopkins, P. E. Contributions of Inter- and Intraband Excitations to Electron Heat Capacity and Electron-Phonon Coupling in Noble Metals. *J. Heat Transfer* **2010**, *132*, 014504.

(36) Choi, D.; Kim, Y. S.; Son, Y. Recovery of indium tin oxide (ITO) and glass plate from discarded TFT-LCD panels using an electrochemical method and acid treatment. *RSC Adv.* **2014**, *4*, 50975–50980.

TOC Graphic

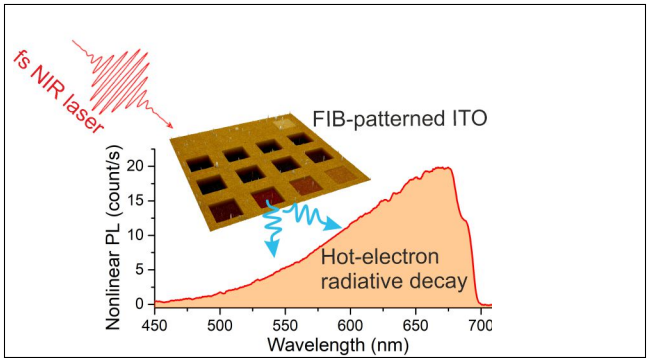
fs NIR laser
FIB-patterned ITO
Hot-electron
radiative decay
Nonlinear PL (count/s)
0
5
10
15
20
450
500
550
600
650
700
Wavelength (nm)